Model-predicted brain temperature computational imaging by multimodal noninvasive functional neuromonitoring of cerebral oxygen metabolism and hemodynamics: MRI-derived and clinical validation

Miaowen Jiang[1],*, Fuzhi Cao[2],*, Qihan Zhang[3],*, Zhengfei Qi[1], Yuan Gao[2], Yang Zhang[3] (ORCID), Baoyin Song[3], Chuanjie Wu[3], Ming Li[4], Yongbo Xu[5], Xin Zhang[6], Yuan Wang[3], Ming Wei[1,5,7] and Xunming Ji[1,3,4] (ORCID)

Abstract

Brain temperature, a crucial yet under-researched neurophysiological parameter, is governed by the equilibrium between cerebral oxygen metabolism and hemodynamics. Therapeutic hypothermia has been demonstrated as an effective intervention for acute brain injuries, enhancing survival rates and prognosis. The success of this treatment hinges on the precise regulation of brain temperature. However, the absence of comprehensive brain temperature monitoring methods during therapy, combined with a limited understanding of human brain heat transmission mechanisms, significantly hampers the advancement of hypothermia-based neuroprotective therapies. Leveraging the principles of bioheat transfer and MRI technology, this study conducted quantitative analyses of brain heat transfer during mild hypothermia therapy. Utilizing MRI, we reconstructed brain structures, estimated cerebral blood flow and oxygen consumption parameters, and developed a brain temperature calculation model founded on bioheat transfer theory. Employing computational cerebral hemodynamic simulation analysis, we established an intracranial arterial fluid dynamics model to predict brain temperature variations across different therapeutic hypothermia modalities. We introduce a noninvasive, spatially resolved, and optimized mathematical bio-heat model that synergizes model-predicted and MRI-derived data for brain temperature prediction and imaging. Our findings reveal that the brain temperature images generated by our model reflect distinct spatial variations across individual participants, aligning with experimentally observed temperatures.

[1]Beijing Institute for Brain Disorders, Capital Medical University, Beijing, 100069, China
[2]School of Engineering Medicine, Beihang University, Beijing 100083, China
[3]Department of Neurology and Neurosurgery, Xuanwu Hospital, Capital Medical University, Beijing 100053, China
[4]China-America Institute of Neuroscience and Beijing Institute of Geriatrics, Xuanwu Hospital, Capital Medical University, Beijing 100053, China
[5]Clinical College of Neurology, Neurosurgery and Neurorehabilitation, Tianjin Medical University, Tianjin 300203, China
[6]Brainnetome Center, Laboratory of Brain Atlas and Brain-inspired Intelligence, Institute of Automation, Chinese Academy of Sciences, Beijing 100190, China

[7]Tianjin University, Tianjin Huanhu Hospital, Tianjin 300203, China

*These authors contributed equally to this work.

Corresponding authors:
Xunming Ji, NO 45, Changchun Street, Xicheng District, Beijing 100053, China.
Email: jixm@ccmu.edu.cn

Ming Wei, NO 22, Qixiangtai Road, Heping District, Tianjin 300203, China.
Email: drweiming@163.com

Yuan Wang, NO 45, Changchun Street, Xicheng District, Beijing 100053, China.
Email: wilma0106@163.com

Introduction

Brain temperature, influenced by neural activity, cerebral circulation, and neuroinflammation,[1,2] serves as a vital physiological indicator in diagnosing neurological diseases. Its rhythmic patterns can predict the survival rate of brain injury,[3] and thermoregulation is linked to patient outcomes.[4] Furthermore, brain temperature is a key parameter in targeted temperature management (TTM) within the therapeutic hypothermia strategy for treating severe neurological diseases, such as acute ischemic stroke (AIS),[5] intracerebral hemorrhage (ICH),[6] and traumatic brain injury (TBI).[7] This approach can provide long-term neuroprotection, mitigate neuroinflammation,[8] and induce the production of neuroprotective proteins, like RNA-binding protein RBM3).[9]

However, the application of brain temperature in diagnosis and treatment is limited due to the lack of reliable, direct, real-time, non-invasive brain thermometry techniques for local hypothermia brain tissue in clinical settings.[4,10] Direct-invasive brain thermometry, using a multi-parameter catheter[11] or implantable biosensor,[12] enables real-time measurements in patients with ICH and TBI. However, its practicality and feasibility are constrained in AIS cases.[10] Brain thermometry modalities based on temperature-sensitive magnetic resonance (MR), including magnetization transfer,[13] diffusion,[14,15] proton density,[16] T_1 and T_2 relaxation time,[17] proton resonance frequency (PRF),[18,19] and magnetic resonance spectroscopy (MRS),[20,21] are emerging as promising non-invasive techniques for in vivo brain temperature mapping. Although MR brain thermometry offers precision through phase-difference mapping[22] or chemical shift thermometry[23] (N-acetyl, N-acetyl aspartate (NAA), choline, creatine, and lactate),[24] continuous bedside monitoring remains impractical, especially during endovascular cooling for AIS patients.[25,26] Non-invasive radiometric thermometry[27] and microwave radiometry[28,29] offer the potential for real-time, bedside brain thermometry monitoring, but the accuracy of these methods currently lacks verification.[10]

To enhance our understanding of brain thermoregulation in health and disease, a biophysics model[30] based on Pennes' bioheat equation has been developed for predicting brain temperature.[31–33] Recent research, integrating MR-based measurements of vasculature with a non-simplified anatomical approach, has significantly advanced the precision of thermal modeling with higher fidelity.[4,34,35] Our prior work introduced a bioheat transfer model that utilized the finite element difference method to improve predictions and provide spatially resolved distributions of brain temperature.[36]

The quantitative description and real-time monitoring of brain tissue temperature under therapeutic hypothermia (TH) are essential for assessing heat transfer effectiveness and are considered the most critical parameters by clinicians.[28] The multi-modal brain temperature monitoring system, using near-infrared spectroscopy (NIRS), offers a robust tool for multimodal, non-invasive brain temperature monitoring.[37–40]

To enhance the fidelity and clinical applicability of this biophysics model, our study introduces a noninvasive and spatially resolved method for predicting and imaging brain temperature. As shown in the Figure 1(a), this method comprises construction, analysis and imaging of brain temperature prediction model, mainly including:

1. constructing a bio-heat model that accounts for temperature-dependence;
2. combining multimodal neuromonitoring with theoretical calculations of cerebral metabolic rate of oxygen (CMRO$_2$) and cerebral blood flow (CBF);
3. employing computational fluid dynamics (CFD) to focus on arterial blood temperature;
4. generating whole and regional brain temperature MRI-derived images through linear interpolation of temperature values.

Moreover, a retrospective study involving three patients with MCA occlusion-induced acute ischemic stroke (AIS), who underwent short-duration intravascular hypothermia therapy targeted to the ischemic territory in conjunction with mechanical thrombectomy (MT), was conducted to produce localized brain temperature imaging in the infarct region. This research is essential for the incorporation of brain temperature into clinical decision-making, since it will offer theoretical backing for the creation of devices that detect brain temperature in real-time, non-invasively at the bedside. Furthermore, it will be beneficial to forecast and assess the clinical prognosis if hypothermia treatment is optimized based on the rule of brain temperature change.

Materials and methods

From each subject, as shown in the Figure 1(a), to facilitate personalized brain temperature imaging based on this bioheat model, we analyzed data from intravascular hypothermia therapy in AIS patients. This enabled us to achieve brain temperature imaging of the infarcted MCA regions at various stages of the hypothermia procedure. To enhance the model's high fidelity and clinical practicability, this study introduces a noninvasive and spatially resolved method for brain temperature prediction and imaging. Our bio-heat model advances the characterization of thermal responses in both healthy and injured brains, incorporating individual variability as a pivotal step towards personalized brain temperature predictions. This proof-of-concept study suggests potential inter-individual variations in brain
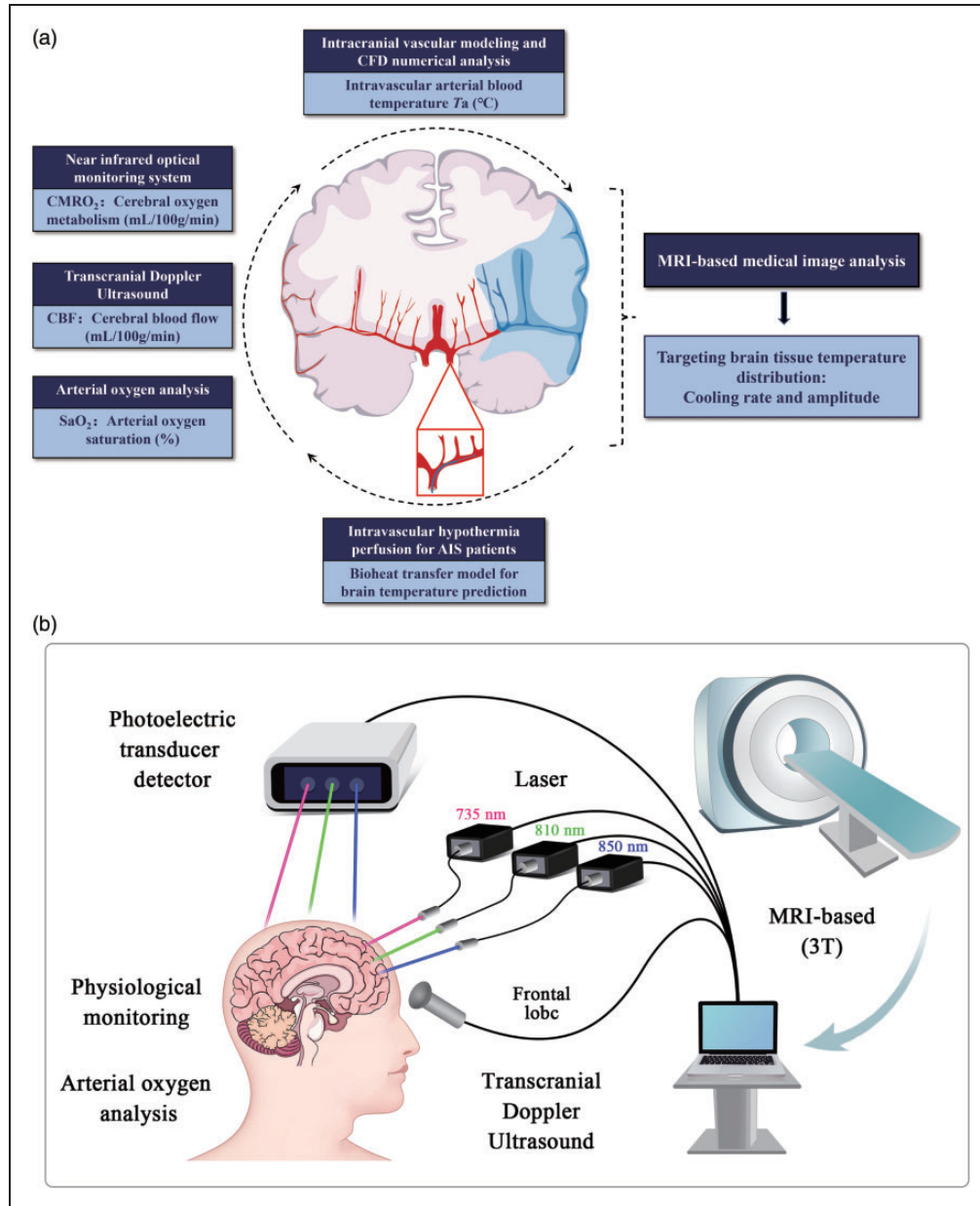
Figure 1. (a) The process of the spatially resolved brain temperature prediction and imaging method, which primarily comprises bioheat model conduction, multimodal neuromonitoring, cerebral hemodynamics CFD, and MRI image analysis and (b) the multimodal neuromonitoring system, integrated with MRI data, primarily includes: NIRS for regional cerebral oxygen saturation (rSO$_2$), transcranial doppler ultrasound (TCD) for CBF-velocity, and other physical parameters such as peripheral oxygen saturation.

temperature, thereby encouraging further research to thoroughly understand these differences for clinical use.

Bioheat model of brain temperature

The Pennes' bioheat model. The bio-heat model of brain temperature was conducted with considerations of the temperature-dependence on metabolism heat $q_m\left(\frac{W}{m^3}\right)$, volumetric perfusion rate $\omega_1\left(\frac{ml}{min\cdot100g}\right)$, and perfusion temperature T_a (°C) of brain tissue. (Figure 1)

Additionally, the impact of geographical location M (spherical coordinate system, M (r, θ, φ)) on heat transport in brain tissue and the transient changes in brain tissue temperature due to variations in cooling time. The formula for the bioheat model of brain temperature T is as follows:

$$\rho_t c_t \frac{\partial T}{\partial t} = \frac{\lambda_t}{r^2} \cdot \frac{\partial}{\partial r}\left(r^2 \cdot \frac{\partial T}{\partial r}\right) + \rho_b c_b \omega_1 (T_a - T) + q_m$$

(1)

where $\rho_t \left(\frac{kg}{m^3}\right)$ represents brain tissue density, $c_t \left(\frac{J}{Kg \cdot K}\right)$ denotes the specific heat capacity of brain tissue, $\lambda_t \left(\frac{W}{K \cdot m}\right)$ is the thermal conductivity of brain tissue, $\rho_b \left(\frac{kg}{m^3}\right)$ signifies blood density, $c_b \left(\frac{J}{Kg \cdot K}\right)$ is the blood's specific heat capacity.

The bioheat model's partial differential equation was numerically solved using the explicit finite difference method. MATLAB (2016 R, MathWorks. Inc, USA) was employed to program the model's solution. The process of solving the model involved:

(i) Differential time domain analysis of brain temperature:

$$\frac{\partial T}{\partial t} = \frac{T(i+1,j) - T(i,j)}{\rho_t \cdot c_t \cdot \Delta t} = \frac{1}{\rho_t \cdot c_t \cdot \Delta t}$$

$$\left\{ \begin{array}{l} \frac{\lambda_t}{r^2} \cdot \frac{\partial}{\partial r} \cdot \left[r^2 \cdot \frac{\partial T(i+1,j) - \partial T(i,j)}{\partial r} \right] \\ + \rho_b \cdot c_b \cdot \alpha \cdot \omega_0 \\ \cdot \left[T_a - T(i+1,j) + T(i,j) \right] + q_0 \cdot 3^{\frac{T-37}{10}} \end{array} \right\} \quad (2)$$

(ii) Spatial difference domain analysis of brain temperature, the analytic process for θ and φ were the same as r:

$$\frac{\partial T}{\partial r} = \frac{T(i,j+1) - T(i,j)}{\rho_t \cdot c_t \cdot \Delta r} = \frac{1}{\rho_t \cdot c_t \cdot \Delta r}$$

$$\left\{ \begin{array}{l} \frac{\lambda_t}{r^2} \cdot \frac{\partial}{\partial r} \cdot \left[r^2 \cdot \frac{\partial T(i,j+1) - \partial T(i,j)}{\partial r} \right] + \rho_b \cdot c_b \cdot \alpha \cdot \omega_0 \\ \cdot \left[T_a - T(i,j+1) + T(i,j) \right] + q_0 \cdot 3^{\frac{T-37}{10}} \end{array} \right\} \quad (3)$$

$$\frac{\partial^2 T}{\partial r^2} = \frac{T(i,j+1) - 2T(i,j) + T(i,j-1)}{\rho_t \cdot c_t \cdot (\Delta r)^2} = \frac{1}{\rho_t \cdot c_t \cdot (\Delta r)^2}$$

$$\left\{ \begin{array}{l} \frac{\lambda_t}{r^2} \frac{\partial}{\partial r} \cdot \left[r^2 \cdot \frac{\partial T(i,j+1) - 2\partial T(i,j) + \partial T(i,j-1)}{\partial r} \right] \\ + \rho_b \cdot c_b \cdot \alpha \cdot \omega_0 \cdot \left[T_a - T(i,j+1) + 2T(i,j) - T(i,j-1) \right] \\ + q_0 \cdot 3^{\frac{T-37}{10}} \end{array} \right\} \quad (4)$$

Blood perfusion and metabolic rate of healthy and ischemic brain tissue. Healthy and ischemic brain tissues exhibit markedly different blood perfusion and metabolic rates, at 25% and 30% respectively. These normal values were attained by analyzing blood perfusion and metabolic rate in the ischemic core during ischemia. The developing infarct, or ischemic penumbra, showed reduced blood perfusion and metabolic rate to 40% and 50%, respectively.[41]

$$\omega = \min(\omega_c, 0.25\omega_0), (ischemic\ core)\ and$$
$$= min(\omega_c, 0.4\omega_0), (ischemic\ penumbra) \quad (5)$$

$$q = \min(q_c, 0.3q_0), (ischemic\ core)\ and$$
$$= min(q_c, 0.5q_0), (ischemic\ penumbra) \quad (6)$$

where ω_0 and q_0 represent the blood perfusion and metabolic rates, respectively, under normal conditions (37°C) and ω_c and q_c are temperature-adjusted parameters derived from our preliminary study.[42]

Calculation of cerebral metabolic heat production. To $CMRO_2$ quantification based on the modified Fick principle,[43]

$$CMRO_2 = k \times [Hb] \times CBF \times OEF \quad (7)$$

the factor describing the quantity of O_2 bound to fully saturated hemoglobin concentration (Hb) was k = 1.39 $(ml(O_2)/g(Hb))$,[44] where OEF represents the oxygen extraction fraction. Consequently, cerebral metabolic heat production q_m can be quantified,[43–45]

$$q_m = \propto \times k \times [Hb] \times CBF \times R \times \frac{4}{3}(S_aO_2 - rSO_2) \quad (8)$$

where $\propto$ is the infarct volume influence coefficient. The cerebral metabolic rate of oxygen ($CMRO_2$) was estimated to be $3 \sim 3.5 \, ml/(min \cdot 100 \, g)$, resulting in a cerebral metabolic heat production of approximately $0.6 \, J/(g \cdot min)$[46] SaO_2 denotes arterial blood oxygen saturation, rSO_2 represents regional cerebral tissue oxygen saturation (StO_2), and R is the ratio of small to large vessel hematocrit, set at $0.5 \sim 0.75$.[47]

Multimodal neuromonitoring system

The system composition. As depicted in Figure 1(b), the multimodal neuromonitoring system was established to measure rSO_2 and CBF in healthy individuals, providing baseline data for the key parameters of this bio-heat model. Peripheral oxygen saturation and physical parameters for each subject were monitored using a multiparameter patient monitor designed for hospital use (ePM12, Shenzhen Mindray Bio-Medical Electronics Co., Ltd., Shenzhen, China). Resting CBF metrics were recorded via Transcranial Doppler sonography (HI VISION Ascendus, Hitachi, Ltd., Japan) by an experienced sonographer in all participants. The NIRS

system for rSO2 monitoring employed three wavelengths (735 nm, 810 nm, and 850 nm) of light emitting diodes (LED) sources (SMT735/810/850) for time-multiplexing illumination, based on our preliminary study.[48]

Optical computation of [Hb] in brain by NIRS. The absolute amounts of C_{Hb} and C_{HbO_2} in brain tissue can be determined using the modified three-wavelength Lambert-Beer law[49] to calculate the [Hb] in the brain (Figure 2):

$$OD^{\lambda_1} = \frac{\mu_a^{\lambda_1} L}{ln10} = \left(\varepsilon_{HbO_2}^{\lambda_1} C_{HbO_2} + \varepsilon_{Hb}^{\lambda_1} C_{Hb} \right) L \qquad (9)$$

$$OD^{\lambda_2} = \frac{\mu_a^{\lambda_2} L}{ln10} = \left(\varepsilon_{HbO_2}^{\lambda_2} C_{HbO_2} + \varepsilon_{Hb}^{\lambda_2} C_{Hb} \right) L \qquad (10)$$

$$OD^{\lambda_3} = \frac{\mu_a^{\lambda_3} L}{ln10} = \left(\varepsilon_{HbO_2}^{\lambda_3} C_{HbO_2} + \varepsilon_{Hb}^{\lambda_3} C_{Hb} \right) L \qquad (11)$$

The path length L was not need to calculate, and formulas can be combined with each other to eliminate. The process of eliminating path length L was followed as shown in the Equ.4 and Equ.5:

$$\frac{OD^{\lambda_1}}{OD^{\lambda_2}} = \frac{\mu_a^{\lambda_1}}{\mu_a^{\lambda_2}} = \frac{\varepsilon_{HbO_2}^{\lambda_1} C_{HbO_2} + \varepsilon_{Hb}^{\lambda_1} C_{Hb}}{\varepsilon_{HbO_2}^{\lambda_2} C_{HbO_2} + \varepsilon_{Hb}^{\lambda_2} C_{Hb}} \qquad (12)$$
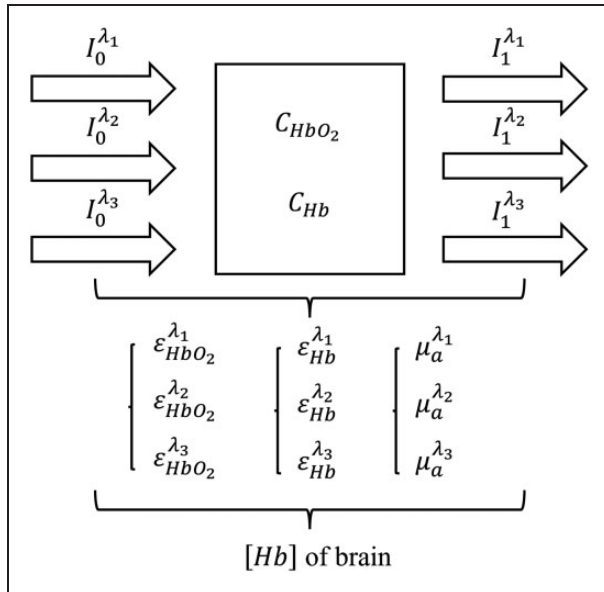

Figure 2. The calculation principle of brain hemoglobin concentration [Hb], defined as [Hb] = C_{HbO2} + C_{Hb}, where C_{HbO2} and C_{Hb} represent the concentrations of oxygenated and deoxygenated hemoglobin in brain tissue, respectively.

$$\frac{OD^{\lambda_1}}{OD^{\lambda_3}} = \frac{\mu_a^{\lambda_1}}{\mu_a^{\lambda_3}} = \frac{\varepsilon_{HbO_2}^{\lambda_1} C_{HbO_2} + \varepsilon_{Hb}^{\lambda_1} C_{Hb}}{\varepsilon_{HbO_2}^{\lambda_2} C_{HbO_2} + \varepsilon_{Hb}^{\lambda_2} C_{Hb}} \qquad (13)$$

Based on the definition of tissue oxygen saturation, [Hb] in the brain can be derived by fitting multiple sets of measured rSO2 data:

$$rSO_2 = \frac{C_{HbO_2}}{C_{HbO_2} + C_{Hb}}$$
$$= \frac{\varepsilon_{Hb}^{\lambda_1} - \varepsilon_{Hb}^{\lambda_2} \frac{\mu_a^{\lambda_1}}{\mu_a^{\lambda_2}}}{\frac{\mu_a^{\lambda_1}}{\mu_a^{\lambda_2}} \left(\varepsilon_{HbO_2}^{\lambda_2} - \varepsilon_{Hb}^{\lambda_2} \right) - \left(\varepsilon_{HbO_2}^{\lambda_1} - \varepsilon_{Hb}^{\lambda_1} \right)} \qquad (14)$$

where OD signifies optical density, λ_i represents wavelengths ($i = 1, 2, 3$), μ_a is the optical attenuation coefficient, ε denotes the extinction coefficient, and L is the average path length of the photon through the tissue.

Multi-physical CFD analysis

3 D CFD model for cerebral hemodynamics. Cerebral hemodynamics, focusing on arterial blood temperature distribution in the intracranial area such as the MCA, employs a mathematical model governed by Navier–Stokes equations and computational fluid dynamics (CFD) methods, with cerebrovascular structures derived from MRI data. As illustrated in Figure 3(a), using the Digital Imaging and Communication in Medicine (DICOM) standard format, the 3D model of intracranial artery vessels was developed for a healthy individual (Preclinic Medical, Shanghai, China). The 3D geometry of cerebrovascular surfaces was reconstructed using software such as Mimics (Materialise NV, Leuven, Belgium) and Geomagic Wrap (Geomagic, North Carolina, USA). The ANSYSICEM CFD meshing program (ANSYS, Inc., USA) was then utilized for further analysis of the vascular surface and creation of the computational domain (volume mesh).

The blood flow was modeled as an incompressible and viscous Newtonian fluid, incorporating the compressibility effects of the vascular wall and heat transmission. Due to the complex geometry, an unstructured tetrahedral cell was employed for domain discretization, with a finer mesh near the vessel wall and at stenosis locations where the flow field was more critical. The vessel wall, assumed to have a thickness of approximately 2.0 mm, was considered a no-slip boundary condition. The initial conditions were set to zero for each example, and the details of the inlet and outflow boundary conditions included the internal carotid artery or vertebral artery for the inlet, and the distal cerebral artery and the temperature of the cold infusate for the outlet, respectively. The convergence criterion
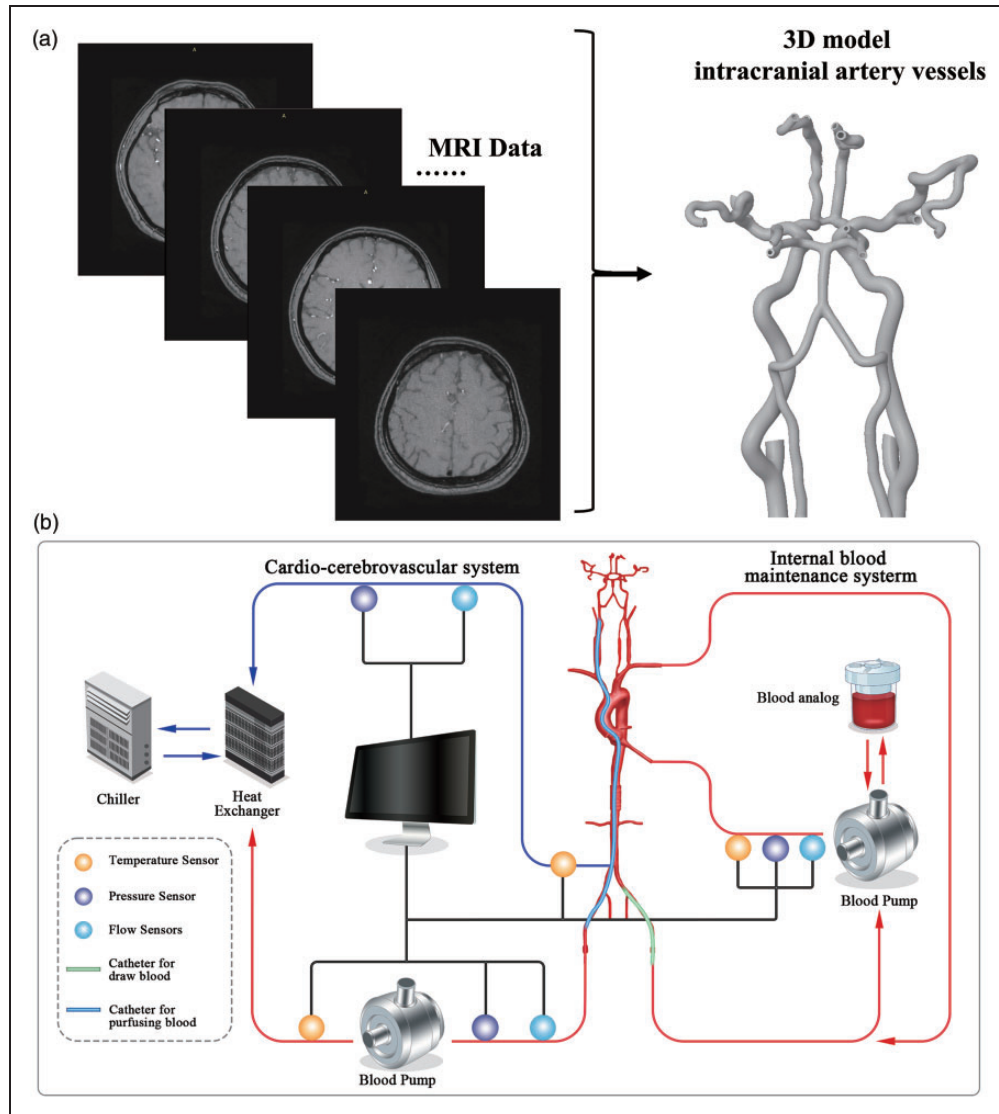
Figure 3. (a) The reconstructed process of the 3D geometry of cerebrovascular surfaces, with cerebrovascular structures acquired from MRI data and (b) The artificial circulatory system constructed, including a blood pump module, sensing module, and blood heat exchanger module.

was set with a relative residual target of root mean square (RMS) at 1.0×10^{-5}, and the blood flow was considered laminar.[50]

The in vitro experiment. The absence of endovascular catheter temperature sensing in interventional instruments often hinders the accurate acquisition of the catheter's exit temperature in clinical practice of intravascular hypothermia therapy, thus limiting the further measurement of intracranial temperature. The artificial circulatory system (Figure 3(b)), developed in our research,[51] was established *in vitro* to measure the delivery temperature of the intravascular hypothermia interventional catheter. This system comprised a blood pump module (Preclinic Medical, Shanghai, China),

a 'pressure-flow' sensing module (FD-XS1; Keyence, Osaka, Japan), and a blood heat exchanger module. The delivery temperature at the catheter's distal tip was monitored using a thermocouple K-type multi-channel temperature tester (AT4204; Applent, Changzhou, Jiangsu, China).

Brain temperature prediction that MRI-derived

By mapping temperature data onto MRI images and employing linear interpolation, brain temperature imaging was created. Based on the Flood Fill algorithm in Matlab-based Image Segmenter toolbox, similar pixels were aggregated into regions according to the grayscale values and spatial position information of

pixels in MRI images, enabling the segmentation of the scalp and infarct areas. Segmented 2D images were converted into volumetric data (voxels) and then reconstructed into detailed 3D meshes of the scalp and infarct regions through surface extraction. A point-based rigid registration algorithm was then employed to estimate the spatial position of the sensor relative to the scalp. This allowed the brain temperature data to be mapped to the 3D MRI space. The temperature within the cerebral infarction region was then interpolated using linear interpolation techniques from the Fieldtrip toolbox in 3D MRI space. Subsequently, the temperature value was projected onto the corresponding MRI section to generate the brain temperature prediction map.

Brain temperature computational imaging that model-predicted

Model construction based the MRI data. Then Raster2Vector software was used to scan the MRI image data to obtain the contours of the brain, and the output of the contours was imported into AutoCAD (Autodesk Computer Aided Design 2020; San Rafael, California, USA) to establish a two-dimensional (2D) geometric model of the brain based on the MRI data. For the entire brain model line segment smooth and consistent, the model border line was made simpler and the cross and tiny angle were removed. Finally, the 2D brain geometric model was imported into Ansys software 2021 R1 (SpaceClaim; ANSYS, Pittsburgh, Pennsylvania, USA) for pre-processing of numerical heat transfer simulation.

Computational imaging through the finite element heat transfer analysis. The cerebral spinal fluid, the skull area, the brain tissue region at low temperature (32°C), and the normal temperature (37.5°C) were all extracted. The temperature was heat transferred from one fluid or solid region to another throughout the conjugate coupling of the four zones. In our preliminary study, physical properties of brain tissue were identified.[36] The triangular mesh was employed for grid division in the 2D brain model. The overall mesh number was 352,232, the minimum orthogonal mass of the mesh was 0.35, and the minimum mesh size was 0.4 mm. The turbulence model with the enlarged wall surface was modeled using the realizable $k-\varepsilon$ model, which was based on the energy equation. A pressure base solver was employed, and the brain tissue and cerebrospinal fluid were designated as incompressible fluids.

By using the continuity equation, the pressure and velocity coupling method was constructed. The absolute velocity was set, the gradient option based on the volume element was selected, and the velocity-pressure coupling problem was solved using the Simplec method. The arithmetic average of nearby nodes was used to determine the interface viscosity coefficient and density. The pressure field was discretized using a normal approach, the others were discretized using a second-order upwind scheme, and the pressure gradient benefit reinforced the wall treatment.

Clinical validation: intravascular hypothermia therapy protocol

This study used retrospective clinical study data, which the clinical study (approval number:2022-161) had been approved by the Ethics Committee of Tianjin Huanhu Hospital and was conducted according to the principles of the Declaration of Helsinki. Written informed consent was obtained from each patient or their legal representative. Treating physicians conducted a comprehensive review of each patient's medical history and meticulously documented symptoms, vital signs, and comorbidities. In addition to blood tests and physical exams, magnetic resonance imaging (MRI) was performed, including MRA and diffusion-weighted imaging (DWI) sequences. Additional diagnostic procedures were also undertaken. All findings were thoroughly documented in the patient's case report file.

For diagnostic angiography, local anesthesia was the preferred method. However, in cases where a patient's agitation level precluded the use of local anesthesia, general anesthesia was administered. Following the identification of significant vascular obstruction, a microcatheter was introduced into the thrombus. Angiographic imaging using the microcatheter verified the patency of the thrombus's distal end. Subsequently, mechanical thrombectomy was performed using the Solitaire FR, or concomitant aspiration thrombectomy as needed. Post successful thrombectomy, angiography confirmed the reopening of previously obstructed channels. Then, 300 ml of Ringer's solution or 4°C saline was infused into the internal carotid artery via the guiding catheter at a consistent rate of 30 ml/min. During the study period, 3 patients met the study criteria. The key baseline characteristics of those patients and their outcomes are shown in the Table. S1 (Supplemental material).

Imaging, including MRA, was performed on 3T MTI system with the following parameters: DWI acquisition parameters using SE-EPI sequence: TR = 2900 ms, TE = 73 ms, section layers = 19, section thickness = 5 mm, intersection gap = 1.5 mm, FOV = 240×240 mm^2, matrix = 168×134, acquisition time = 23 s, reconstruction of ADC mapping. MRA acquisition parameters using 3D-TOF sequence: TR = 21 ms, TE = 3 ms, section layers = 40, section

thickness $= 0.8 \, \text{mm}$, FOV $= 220 \times 172 \, \text{mm}^2$, matrix $= 320 \times 304$, acquisition time $= 23 \, \text{s}$.

Results

A total of 33 healthy adults (16 females and 17 males) participated in the experiment, aged 22–43 years. The average values of age, weight, and height were 35.82 ± 5.98 years, $69.88 \pm 13.18 \, \text{kg}$, and $168.70 \pm 8.10 \, \text{cm}$, respectively. The subjects provided data for multimodal noninvasive monitoring, reported as mean $\pm$ SD values in a brain temperature bioheat model. No significant differences from baseline were observed in SaO2 and rSO2 (Figure 4(a)). The rSO2, discontinuously measured by the neuromonitoring system, was approximately 33 percentage points higher than SaO2, indicating that the relative proportion of

hemoglobin in brain tissue is lower than that in blood. The unilateral CBF volume of the MCA was determined using the formula $FV = MFV \times \pi \times (d/2)^2$, with a representative mean MCA vessel diameter of $3.5 \, \text{mm}$ as measured by TCD[52] (Figure 4(b)). Figure 4 (c) displays the CMRO$_2$ calculated using Equation (7), averaging 6.9662 ± 0.95 (ml/100 g/min) among the subjects. Subsequently, the metabolic heat production of brain tissue corresponding to the MCA region was calculated to be 24253.99 (W/m^3) based on these baselines.

In the 3D hemodynamic simulation, we demonstrated four intravascular temperature heat transfer conditions, each with a different temperature of the cold fluid exiting the interventional catheter infused into intracranial arterial vasculature modeled from healthy MRI data (Figure 4(d)). The intravascular temperature at the unilateral MCA increased with the gradual rise
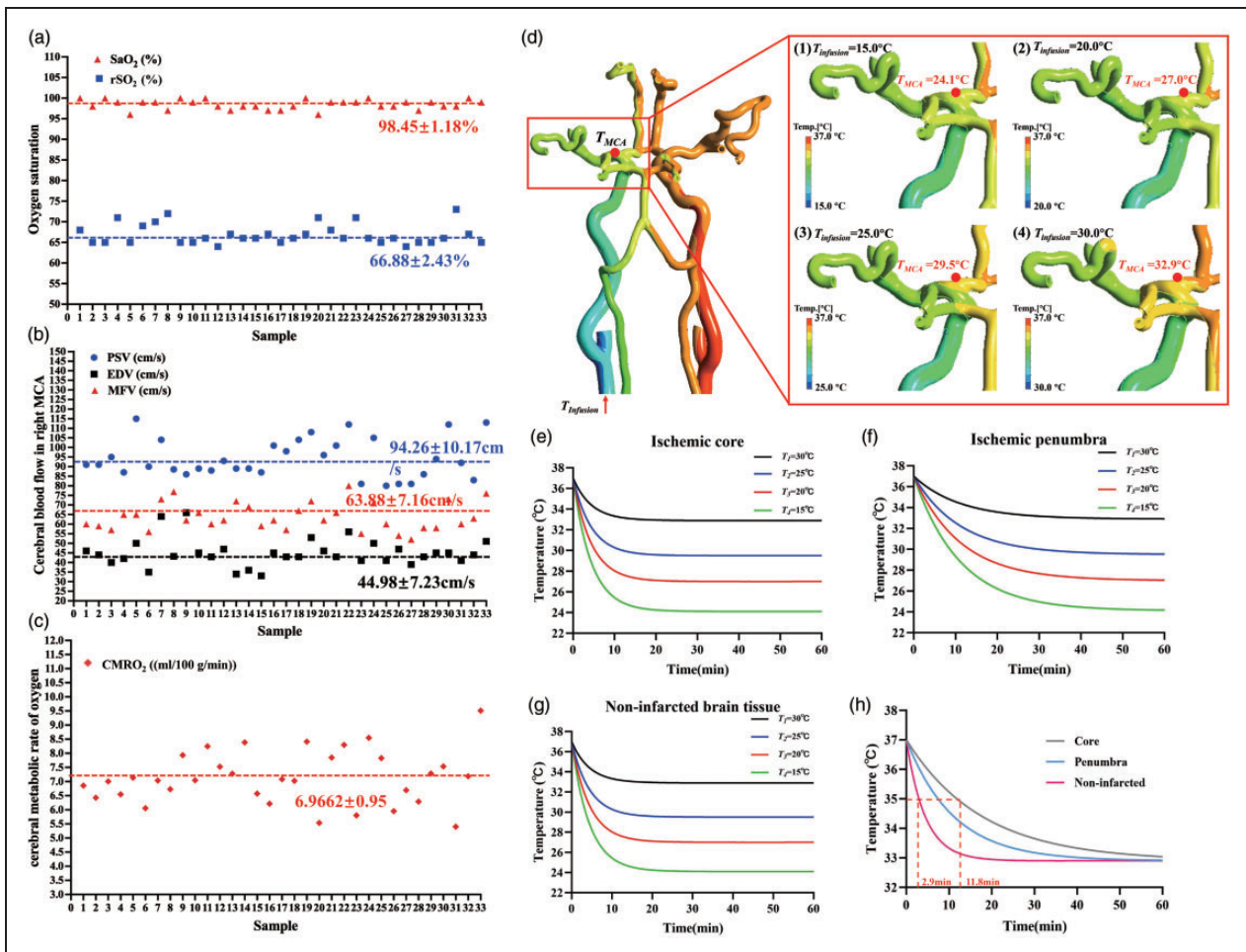

Figure 4. The measurements of multimodal noninvasive monitoring as a baseline in the brain temperature bioheat model: (a) SaO$_2$ and rSO$_2$; (b) PSV (Peak Systolic Velocity), EDV (End-Diastolic Velocity) and MFV (Mean Flow Velocity); (c) CMRO$_2$; (d) The 3D hemodynamic simulation of four intravascular temperature heat transfer conditions with different temperatures (15°C, 20°C, 25°C and 30°C, denoted by T$_1$, T$_2$, T$_3$ and T$_4$, respectively) of the cold fluid exiting the interventional catheter; effects of different infusion temperatures on transient temperature profiles of the (e) ischemic core, (f) penumbra and (g) non-infarcted; (h) transient temperature profiles for the ischemic core, penumbra, and non-infarcted areas at an infusion temperature of 30°C.

in perfusion exit temperature, ranging from 24.1°C to 32.9°C. The cold temperature, with a perfusion flow volume of 20 ml/min, was gradually neutralized by the normal blood flow of 400 ml/min[52] in the bilateral carotid arteries, ensuring that the temperature on the contralateral side remained unaffected.

The integration of baseline neuromonitoring data and hemodynamic temperature distribution with the bioheat transfer model facilitated the numerical prediction of brain temperature during intravascular hypothermia therapy. Figure 4(e) to (h) illustrates the impact of varying perfusion temperatures at the exit of the interventional catheter on transient temperature profiles in both healthy and infarcted brain tissue. Lower infusion temperatures resulted in more rapid induction of hypothermia and reduced brain temperatures, regardless of tissue health. The transient temperature profiles differed markedly between the ischemic core, the penumbra, and non-infarcted tissue for any given infusion temperature. As demonstrated in Figure 4(h), with an infusion temperature of 30°C, hypothermia (35°C) was induced almost four times faster in non-infarcted tissue (2.9 min to reach hypothermia) compared to the ischemic core (11.8 min to reach hypothermia), with the ischemic penumbra temperature being higher than the core but lower than that of non-infarcted tissue.

Assuming a hemispheric shape for the anatomical structure of a head model, with certain tissue layers omitted for simplicity, Figure 5(a) presents the brain in three dimensions. The X-axis includes the ears, the Y-axis is marked by the nose, and the Z-axis follows the central line of the ears, with dimensions -65.5 mm $< x <+65.5$ mm, -72 mm $<y<+$ 72 mm, and $0<z<+124$ mm. The primary outcome of this study was to generate whole brain temperature imaging based on MRI for a healthy individual (Figure 5(b)). The study set the intravascular hypothermia blood temperature at 32°C. Model-predicted brain temperature imaging, conducted over time, qualitatively demonstrated that an infusion rate of 20 ml/min resulted in a decrease of the overall brain temperature from 37°C to 33.6°C, with hypothermia being induced at approximately 30 min.

A retrospective study in three patients with MCA occlusion-induced AIS, who underwent short-duration intravascular hypothermia therapy in conjunction with mechanical thrombectomy (MT), was conducted to generate local brain temperature maps in the infarct region (Figure 5(c) and (d)). Image segmentation lines based on MRI were used to identify the cerebral infarction tissue's spatial region and display the spatial distribution of brain temperature (Figure 5(c)). A simplified brain model's cylindrical coordinate system was established, including $a_1...a_{17}$

for X-axis, $b_1...b_{14}$ for Z-axis, and θ angle, thus pinpointing the infarct core's location. Assuming $\theta = 45°$ for the core of the cerebral infarction region and using the maximum infarct size as the base plane, the segmentation line locations for the three subjects were subject1 ($z = 40$ mm, $l = 32$ mm), subject2 ($z = 15$ mm, $l = 53.9$ mm), and subject3 ($z = 45$ mm, $l = 39.6$ mm), respectively. Based on MRI, the cerebral infarction volume calculation revealed infarct volume influence coefficients of 1/4, 1/2, and 1 for subject1, subject2, and subject3, respectively. Using a simulation platform for an artificial circulatory system, the catheter outlet temperature was measured at $28.8 \pm 0.2°C$ during a 30 ml/min hypothermia infusion. Computational fluid dynamics (CFD) determined the intravascular blood temperature to be $33.6 \pm 0.2°C$.

During a 10-min hypothermia session, local brain temperatures at the infarct core for subject 1 were 36.8°C, 36.6°C, and 36.3°C at 1 min, 5 min, and 10 min, respectively; for subject 2, they were 36.8°C, 36.3°C, 35.8°C; and for subject 3, 36.7°C, 35.8°C, 34.8°C (Figure 5(d)). Thus, it was observed that smaller infarct volumes correlated with higher cooling efficiency in brain tissue. To validate the clinical efficacy of therapeutic hypothermia in our model, we reviewed three AIS patients treated with intravascular hypothermia therapy. Post diagnostic angiography and administration of 4°C cold fluid, the ipsilateral thrombectomy side's auditory temperature was meticulously recorded using a tympanic thermometer, resulting in temperatures of 35.8°C, 35.8°C, and 36.2°C for subjects 1, 2, and 3, respectively.

We proposed a computational brain temperature imaging method based on finite element heat transfer analysis, as shown in Figure 6, in addition to the previous model prediction findings. After the creation of the MRI-based 2D brain tissue model, a FEA-based computational heat transfer was applied to accomplish temperature dispersion and computational mapping during local cooling of brain tissue.

MRI scans of fuzzy intracranial brain tissue were resized to a higher resolution, and the color tone of the images was changed to highlight the important details. In order to achieve an equitable distribution of features (skull, white matter, gray matter, and cerebrospinal fluid) in the processed MRI pictures, the erroneous images were removed and restored (Figure 6(a)). Using a FEA-based computational heat transfer, the temperature distribution and computational mapping during local cooling of brain tissue were accomplished (Figure 6(b)). The targeted low temperature zone covered the cerebral hemisphere of the infarction side for 30 minutes, maintaining a moderate hypothermia condition for subjects 1, 2, and 3. During the 30-minute cooling period, the non-perfused brain
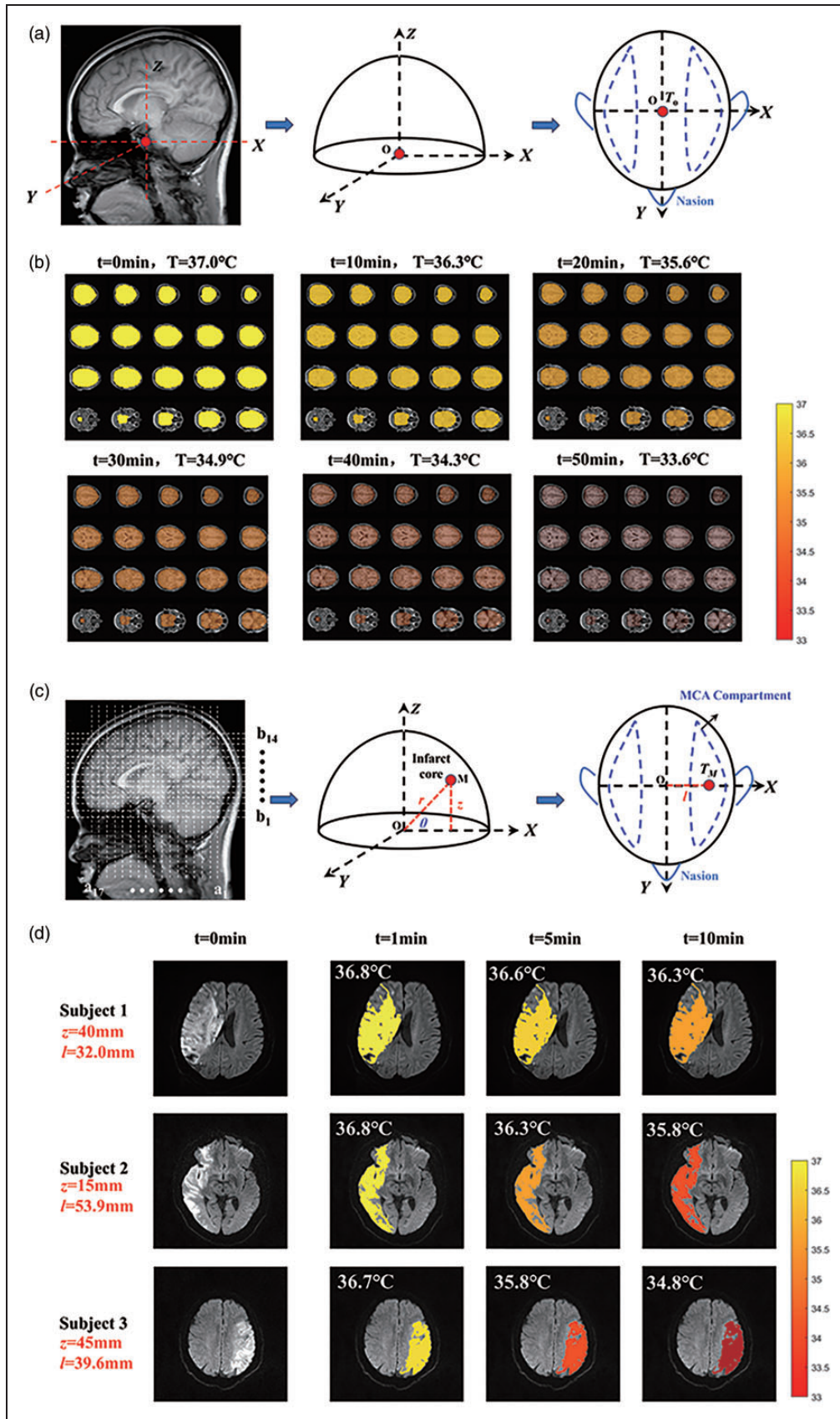
Figure 5. The whole brain temperature imaging based on MRI. (a) the simplified three-dimensional anatomical structure of a head model; (b) model-predicted brain temperature imaging across different brain regions over time. The local brain temperature imaging based on MRI for patients with AIS. (c) the anatomical structure in a simplified cylindrical coordinate system of a head model and (d) model-predicted brain temperature imaging in the cerebral infarction region at different infarct volume influence coefficients during a 10-min intravascular hypothermia therapy session.
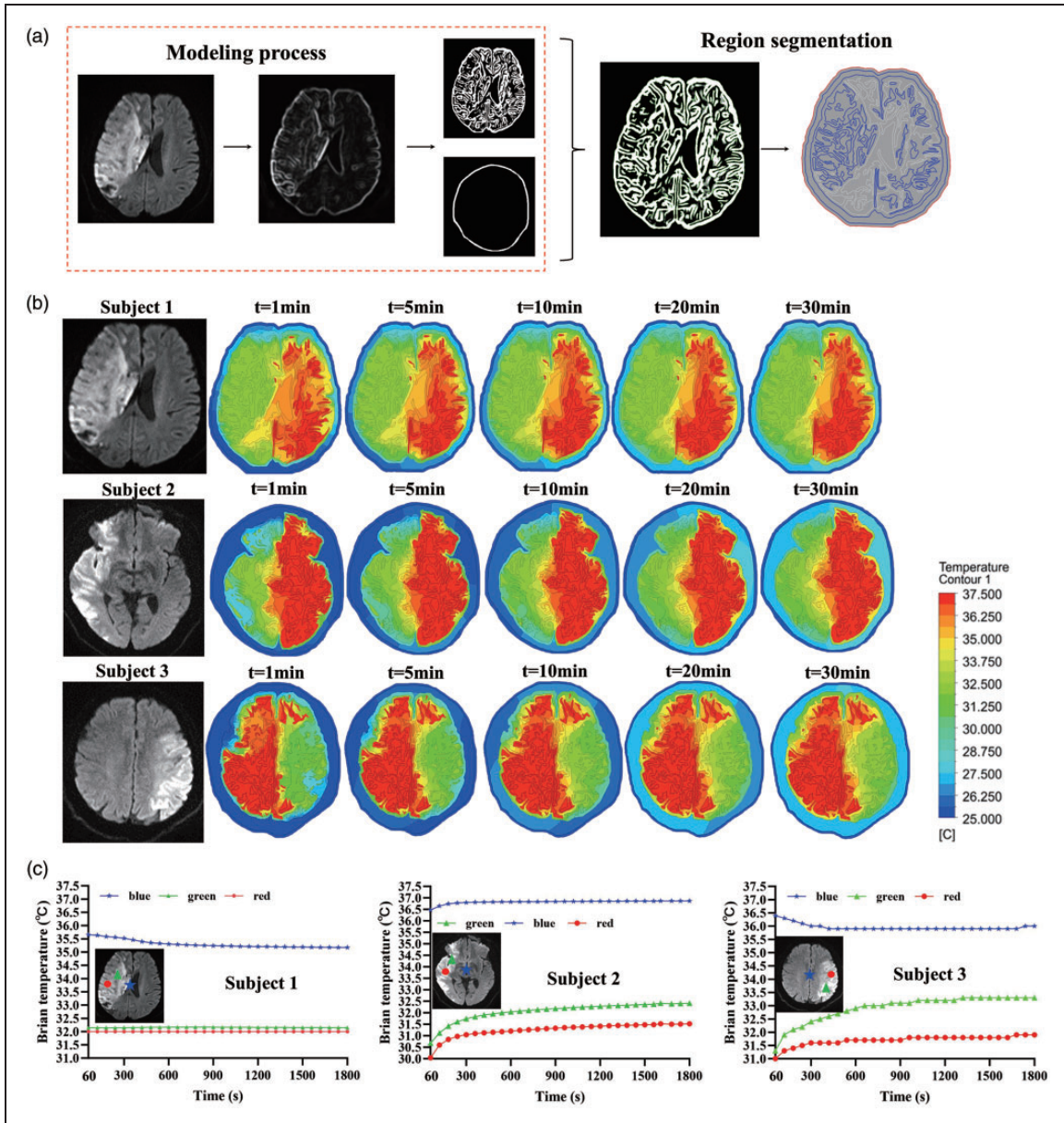
Figure 6. The brain temperature computational imaging based on MRI for patients with AIS. (a) The process of 2D brain model construction based the MRI data; (b) the brain temperature imaging by FEA at different infarct volume influence coefficients during the 30-min hypothermia and (c) the brain temperature curve over time at different points, including the central point of the brain tissue (blue) and two points in the targeted low temperature region (red and green).

region's temperature stayed between 35 and 37.5°C. As shown in Figure 6(c), we select the central point of the brain tissue (blue) and two points in the targeted low temperature region (red and green). The temperature at the central location of the brain tissue dropped by 0.5°C, whereas subject 1's mild hypothermia zone remained stable at about 32°C. Throughout the 60 s to 1800 s, subject 2's low temperature zone had a 1°C increase in temperature, whereas the center of the brain tissue saw a 0.5°C increase. For the subject 3, throughout the same time span, there was a 2°C

increase in the low temperature area, a 1°C rise in the red spot, and a 1°C decrease in the center point of the brain tissue.

Discussion

Model-predicted and MRI-derived brain temperature bio-heat model

We implemented an optimized mathematical model for brain temperature heat transfer (equation (1)), this

study was carried out from the following aspects:

1. It was aimed at the real modeling of intracranial arteriovenous vessels and brain tissue structure, the multidimensional heat transfer mechanism of "blood-brain tissue" based on computational hemodynamic heat transfer was studied, so as to obtain the hydrodynamic spatial field analysis of cerebral blood flow and realize the accurate quantitative analysis of cerebral blood flow and temperature field at the three-dimensional spatial level;

2. It has established and expanded the calculation model of brain temperature heat transfer based on the coupling effect of cerebral hemodynamics and cerebral oxygen metabolism, explored the coupling correlation mechanism of "cerebral blood flow, cerebral oxygen metabolism and brain temperature", and used the three-dimensional modeling of cerebral blood flow as a carrier to engender spatial location information of brain temperature.

Unlike the overly simplistic Pennes's model, our model's innovation stems from the non-invasive monitoring and collection of real brain function parameters from healthy individuals. This approach facilitated the creation of a reliable and authentic baseline database for 'cerebral oxygen-cerebral blood flow.' We integrated an influence coefficient, accounting for varying degrees of brain injury, to accurately assess brain temperature distribution. Our model accounts for both transient temperature changes in brain tissue as a function of cooling time(t) and the impact of heat transfer on tissue depth (r) during hypothermia.

The temperatures predicted by our model consistently align with the range observed in MR-measured temperature distributions, showing no significant bias.[4] Diverging from traditional numerical evaluations and analyses of brain temperature, our study merges MRI image processing technology with a numerical brain temperature model to create MRI-derived 'whole-local' brain temperature imaging. Moreover, our approach considers the extent of brain tissue damage in patients with brain injuries, such as the infarct

volume influence coefficient. We equated its impact on the metabolic capacity and blood perfusion capability of the brain tissue to its proportion in the brain tissue,[53] influencing both metabolic heat production and the efficacy of brain cooling. Hence, we demonstrate the feasibility of making accurate, individualized brain temperature predictions for each patient.

As indicated in Table 1, comparisons of brain temperature models under various hypothermia methods reveal that intravascular hypothermia is markedly more efficient than surface hypothermia. Notably, the intravascular hypothermia model by Lutz et al.[56] exhibited significantly lower cooling efficiency compared to previous models, primarily due to its omission of metabolic considerations.

Cerebral oxygen metabolism

The metabolic heat production of brain tissue in the MCA region was calculated to be 24253.99 W/m^3, surpassing the 16700 W/m^3 typically observed in gray matter.[32] Our model predicated that moderate hypothermia could be induced in the ipsilateral brain hemispheres within 2.7 min, significantly quicker than the 10 min reported in the Konstas' study.[32] This suggests that patients with higher metabolic capacities can achieve hypothermic brain temperatures more rapidly and with greater cooling efficiency. Therefore, it is crucial to consider individual brain oxygen characteristics when developing therapeutic hypothermia strategies for future clinical applications.

In our study, cerebral metabolic heat production was calculated using CMRO$_2$ quantification based on the modified Fick principle. According to equation (8), changes in rSO$_2$ and SaO$_2$, measured by time-resolved near-infrared (TR-NIR), were determined by the equilibrium between oxygen delivery and CMRO$_2$ when the same brain region was continuously monitored in the same subject. This provided a comprehensive view of cerebral oxygen supply and consumption. In contrast, SaO$_2$ solely reflects information about oxygen supply as it monitors only arterial blood. Notably, rSO$_2$ was found to be nearly 20% lower than SaO$_2$, as rSO$_2$ is

Table 1. Comparison of different brain temperature bio-heat models.

Author	Hypothermia method	Cooling efficiency on brain	Induced hypothermia time (35°C)	Imaging or not based MRI
Baker et al.[34]	Intravascular hypothermia therapy	0.37°C/min	5.35 min	No
Konstas. et al[32]	Intravascular hypothermia therapy	0.2°C/min	10 min	No
Katisha. et al.[54]	Whole body surface hypothermia	0.02°C/min	100 min	No
Yin. et al.[55]	Head and neck surface hypothermia	0.016°C/min	125 min	No
Lutz. et al.[56]	Intravascular hypothermia therapy	0.04°C/min	50 min	No
Our model	Intravascular hypothermia therapy	0.74°C/min	2.7 min	Yes

derived from hemoglobin saturation in a mix of arterial, venous, and capillary blood within cerebral tissue.[57]

The detection depth of non-invasive brain oxygen optics was about 25 mm,[48] so temperature monitoring of inner brain regions is not yet possible. In the preliminary study about the brain temperature model by our group[36], under the same perfusion volume at the same time, the temperature change at different depths had little difference with the depth change of brain tissue, but gradually recovered to the ambient temperature at the boundary, which means that the inner brain regions temperature can be estimated with the brain temperature model prediction and the surface temperature monitoring.

Cerebral hemodynamics

Cerebral hemodynamics in this study were primarily divided into two parts:

1. Our modeling approach incorporated the perfusion temperature (T_a), affected by varying cooling temperatures at the catheter's distal tip. This temperature, reconstructed using MRI to map intracranial vascular structures, can approximate the actual temperature with accurate model inputs. Based on CFD analysis, this approach was first introduced by Lagendijk.[58] and considers the perfusion temperature (T_a) in targeted cerebrovascular segments, influenced by blood temperature and velocity, as well as the structural and physical properties of blood vessels. Theoretically, this temperature acts as a radiative source, aiding in the cooling of deeper brain tissues and subsequently impacting brain tissue metabolism.[59] Neuroprotection through TH is temperature-dependent, as a 1°C reduction in brain temperature can reduce the metabolic rate by 7%–10%.[60]

2. CBF, a non-invasive brain parameter, significantly influences $CMRO_2$ (equation (7)) and volumetric perfusion rate (equation (1)). Our model can simulate the effects of hypothermia on the brain, aiding in the interpretation of bedside recordings. According to the Russell-Buckland's model,[61] cerebral metabolism is expected to decrease by 5.1%, blood flow to reduce by 1.1%, and $CMRO_2$ to increase by 2.3% during hypothermia. Alongside the real-time monitoring of CBF via Transcranial Doppler (TCD), as mentioned in the study, the Time-Resolved Near-Infrared (TR-NIR) system, employing a bolus-tracking method with indocyanine green (ICG) as an intravascular flow tracer,[38] also measures CBF. Thus, integrating TR-NIR systems for real-time monitoring of $CMRO_2$ and CBF can reduce costs and enhance the efficiency of

neurological monitoring at the bedside in neuro-intensive care during brain cooling.[62]

Clinical application and limitations

Brain thermal modeling using patient-derived MR could significantly impact clinical care, particularly in scenarios where brain temperature plays a vital role in treatment stratification or prognosis, such as in therapeutic hypothermia[63] and thermal ablation.[64] Our model elucidates the influence of cerebral oxygen metabolism and cerebral blood flow on brain temperature. As healthcare moves towards personalization, this biophysical model, capable of providing individualized predictions, may prove valuable in prognosis, therapy stratification, and patient monitoring. Personalized temperature control could enhance the effectiveness of these novel interventions, notably thermal therapies post-illness or injury, which are often underutilized and yield variable success rates.[65–66]

In addition to the previous model prediction findings, we propose a computational brain temperature imaging technique based on finite element heat transport analysis. The MRI-based 2D brain tissue model was developed, and the FEA-based computational heat transfer was used to accomplish temperature distribution and computational mapping during local cooling of brain tissue. It is possible to quantitatively quantify the temperature at the depth of brain tissue using this approach. The temperature in the depths of the brain tissue varied significantly from the surface temperature, and the cerebral cortex was unable to forecast or reflect the temperature in the core of the brain tissue.

In the study of intravascular hypothermia therapy, the clinical standard operations limit the real-time monitoring of patients' cerebral blood flow and oxygen levels, necessitating the use of a temperature-sensitive numerical prediction model. Furthermore, the inability to monitor the outlet temperature of the catheter in real time—owing to the lack of a clinically approved intravascular hypothermia interventional catheter with temperature sensing—compromises the accuracy of predicting patients' brain temperatures. This study indirectly replaced the validation of brain temperature by real-time monitoring of patients' tympanic membrane temperature. This approach can indirectly show the degree and trend of brain tissue cooling during the neuro-interventional therapy, even if it cannot precisely reflect brain tissue temperature as MRS, which was employed to monitor brain temperature, can. Tympanic membrane temperature decreased by around 2°C in the AIS patients treated with hypothermia in this investigation, which was marginally below the cooling scale determined by the model.

In the future, in order to offer real-time brain temperature monitoring and clinical validation during hypothermia therapy, we will develop brain temperature measuring devices based on the multi-modal monitoring technique and brain temperature prediction model from this study.

Conclusion

In this study, the prediction model of brain temperature was verified and numerically analyzed based on multi-modal neural monitoring technology ("cerebral blood flow", "cerebral oxygen" and "brain temperature (body temperature substitution)") of healthy people, and the accurate quantitative analysis of cerebral blood flow field and temperature field in three-dimensional space was realized. Finally, spatial brain temperature parameters were mapped based on MRI data to realize brain temperature derived imaging with spatial position information, and to realize the surmounting of mathematical model to brain temperature imaging.

Different from diffusion weighted imaging to estimate whole brain temperature by MRI, through the multi-modal neural monitoring technology (such as TCD for CBF and NIRs for StO$_2$), this study aimed to realize the feasibility for real-time, non-invasive and bedside monitoring of brain temperature during the intravascular hypothermia therapy.

Moreover, diffusion weighted temperature imaging technology has higher resolution, and the method in this study can be combined with it in the future to improve the accuracy of the prediction model of brain temperature.

Therapeutic hypothermia has been established as an effective treatment for hypoxic ischemic encephalopathy, with precise brain temperature control being crucial for its success. This study addressed the challenge of quantifying the human brain's heat transport mechanism during mild hypothermia by undertaking the following tasks:

1. Utilizing non-invasive multimodal neural monitoring technology, we reconstructed CBF parameters and cerebral oxygen metabolism heat production values. We then developed a quantitative brain temperature calculation model based on CBF, integrating bioheat transfer theory and an efficient symmetric semi-implicit difference algorithm, achieving high stability and accuracy in brain temperature computations.
2. Focused on quantifying the thermal effects of the cerebral vascular network, we established a computational hemodynamic analysis model for intracranial arteries. This model simulated and analyzed the thermal effects of different mild hypothermia treatment conditions, refrigeration boundary conditions, and vascular network characteristics on brain temperature cooling. It also identified the spatial heterogeneity in the impact of the cerebral vascular network on brain cooling efficiency.
3. Employing MRI imaging technologies, we realized brain temperature imaging for AIS patients. By constructing a brain structure model, brain blood oxygen parameters, and a three-dimensional brain temperature calculation model, we partially uncovered the thermal effects of cerebral vascular network heat transport on mild hypothermia therapy. We put forward a computational brain temperature imaging approach based on finite element heat transfer analysis. The visualization of brain tissue temperature under hypothermia has been achieved. This provides a reference for designing personalized and precisely targeted mild hypothermia treatments.

Authors' contributions

XJ, MW and YW: Conception and design, Acquisition of data, Analysis and interpretation of data, Drafting, revising, and finalizing the article; MJ, FC and QZ: Conception and design, Acquisition of data, Analysis and interpretation of data, Drafting and revising the article; ZQ, YG and YZ: Acquisition of data, Analysis and interpretation of data, Editing the article; BS, CW, ML, YX and XZ: Acquisition of data, Analysis and interpretation of data.

Supplementary material

Supplemental material for this article is available online.

ORCID iDs

Yang Zhang 🔘 https://orcid.org/0000-0002-7857-7147
Xunming Ji 🔘 https://orcid.org/0000-0003-0293-2744

References

1. Sung D, Rejimon A, Allen JW, et al. Predicting brain temperature in humans using bioheat models: Progress and outlook. *J Cereb Blood Flow Metab* 2023; 43: 833–842.

2. Yulug B, Velioglu HA, Sayman D, et al. Brain temperature in healthy and diseased conditions: a review on the special implications of MRS for monitoring brain temperature. *Biomed Pharmacother* 2023; 160: 114287.

3. Rzechorzek NM, Thrippleton MJ, Chappell FM, et al. A daily temperature rhythm in the human brain predicts survival after brain injury. *Brain* 2022; 145: 2031–2048.

4. Sung D, Kottke PA, Risk BB, et al. Personalized predictions and non-invasive imaging of human brain temperature. *Commun Phys* 2021; 4.

5. Geurts M, Petersson J, Brizzi M, et al. COOLIST (cooling for ischemic stroke trial). *Stroke* 2017; 48: 219–221.

6. Baker TS, Durbin J, Troiani Z, et al. Therapeutic hypothermia for intracerebral hemorrhage: systematic review and meta-analysis of the experimental and clinical literature. *Int J Stroke* 2021; 17: 506–516.

7. Docherty A, Emelifeonwu J and Andrews PJD. Hypothermia after traumatic brain injury. *JAMA* 2018; 320: 2204–2206.

8. Yenari MA and Han HS. Neuroprotective mechanisms of hypothermia in brain ischaemia. *Nat Rev Neurosci* 2012; 13: 267–278.

9. VanHook AM. Hypothermia-induced neuroprotection. *Sci Signal* 2017; 10: 10.

10. Horn M, Diprose WK, Pichardo S, et al. Non-invasive brain temperature measurement in acute ischemic stroke. *Front Neurol* 2022; 13: 889214.

11. Huschak G, Hoell T, Hohaus C, et al. Clinical evaluation of a new multiparameter neuromonitoring device: measurement of brain tissue oxygen, brain temperature, and intracranial pressure. *J Neurosurg Anesthesiol* 2009; 21: 155–160.

12. Shin J, Liu Z, Bai W, et al. Bioresorbable optical sensor systems for monitoring of intracranial pressure and temperature. *Sci Adv* 2019; 5: eaaw1899.

13. Prevost VH, Yung A, Morris SR, et al. Temperature dependence and histological correlation of inhomogeneous magnetization transfer and myelin water imaging in ex vivo brain. *NeuroImage* 2021; 236: 118046.

14. Horiuchi D, Shimono T, Tatekawa H, et al. Brain temperature remains stable during the day: a study of diffusion-weighted imaging thermometry in healthy individuals. *Neuroradiology* 2023; 65: 1239–1246.

15. Sai A, Shimono T, Sakai K, et al. Diffusion-weighted imaging thermometry in multiple sclerosis. *J Magn Reson Imaging* 2014; 40: 649–654.

16. Zhu M, Bashir A, Ackerman JJ, et al. Improved calibration technique for in vivo proton MRS thermometry for brain temperature measurement. *Magn Reson Med* 2008; 60: 536–541.

17. Statton BK, Smith J, Finnegan ME, et al. Temperature dependence, accuracy, and repeatability of T(1) and T(2) relaxation times for the ISMRM/NIST system phantom measured using MR fingerprinting. *Magn Reson Med* 2022; 87: 1446–1460.

18. Gaur P, Partanen A, Werner B, et al. Correcting heat-induced chemical shift distortions in proton resonance frequency-shift thermometry. *Magn Reson Med* 2016; 76: 172–182.

19. Wang P. Evaluation of MR thermometry with proton resonance frequency method at 7T. *Quant Imaging Med Surg* 2017; 7: 259–266.

20. Ishida T, Inoue T, Inoue T, et al. Brain temperature measured by magnetic resonance spectroscopy to predict clinical outcome in patients with infarction. *Sensors (Basel, Switzerland)* 2021; 21: 490.

21. Plank JR, Morgan C, Sundram F, et al. Brain temperature as an indicator of neuroinflammation induced by typhoid vaccine: assessment using whole-brain magnetic resonance spectroscopy in a randomised crossover study. *NeuroImage Clin* 2022; 35: 103053.

22. Weis J, Covaciu L, Rubertsson S, et al. Phase-difference and spectroscopic imaging for monitoring of human brain temperature during cooling. *Magn Reson Imaging* 2012; 30: 1505–1511.

23. Dehkharghani S, Mao H, Howell L, et al. Proton resonance frequency chemical shift thermometry: experimental design and validation toward high-resolution noninvasive temperature monitoring and in vivo experience in a nonhuman primate model of acute ischemic stroke. *AJNR Am J Neuroradiol* 2015; 36: 1128–1135.

24. Duijn JH, Matson GB, Maudsley AA, et al. Human brain infarction: proton MR spectroscopy. *Radiology* 1992; 183: 711–718.

25. Chen J, Liu L, Zhang H, et al. Endovascular hypothermia in acute ischemic stroke: pilot study of selective intra-arterial cold saline infusion. *Stroke* 2016; 47: 1933–1935.

26. Wu C, Zhao W, An H, et al. Safety, feasibility, and potential efficacy of intraarterial selective cooling infusion for stroke patients treated with mechanical thrombectomy. *J Cereb Blood Flow Metab* 2018; 38: 2251–2260.

27. Rodrigues DB, Maccarini PF, Salahi S, et al. Design and optimization of an ultra wideband and compact microwave antenna for radiometric monitoring of brain temperature. *IEEE Trans Biomed Eng* 2014; 61: 2154–2160.

28. Groumpas E, Koutsoupidou M, Karanasiou IS, et al. Real-time passive brain monitoring system using near-field microwave radiometry. *IEEE Trans Biomed Eng* 2020; 67: 158–165.

29. Sugiura T, Kouno Y, Hashizume A, et al. Five-band microwave radiometer system for non-invasive measurement of brain temperature in new-born infants: system calibration and its feasibility. *Conf Proc IEEE Eng Med Biol Soc* 2004; 2004: 2292–2295.

30. Zhao G, Panhwar F and Chen Z. Modeling combined cryosurgery and hyperthermia with thermally significant blood vessels. *Theory Appl Heat Transfer Humans* 2018; 2: 669–685.

31. Dagro A and Wilkerson J. A computational investigation of strain concentration in the brain in response to a rapid temperature rise. *J Mech Behav Biomed Mater* 2021; 115: 104228.

32. Konstas A-A, Neimark MA, Laine AF, et al. A theoretical model of selective cooling using intracarotid cold saline infusion in the human brain. *J Appl Physiol (1985)* 2007; 102: 1329–1340.

33. Lutz Y, Loewe A, Meckel S, et al. Combined local hypothermia and recanalization therapy for acute ischemic stroke: estimation of brain and systemic temperature using an energetic numerical model. *J Therm Biol* 2019; 84: 316–322.

34. Baker TS, Zannou AL, Cruz D, et al. Development and clinical validation of a finite element method model mapping focal intracranial cooling. *IEEE Trans Neural Syst Rehabil Eng* 2022; 30: 2168–2174.

35. Lutz Y, Meiner T, Krames L, et al. Selective brain hypothermia for ischemic MCA-M1 stroke: influence of cerebral arterial circulation in a 3D brain temperature model. *IEEE Trans Biomed Eng* 2021; 68: 404–415.

36. Jiang M, Li M, Gao Y, et al. The intra-arterial selective cooling infusion system: a mathematical temperature analysis and in vitro experiments for acute ischemic stroke therapy. *CNS Neurosci Ther* 2022; 28: 1303–1314.

37. Bakhsheshi MF, Diop M, St Lawrence K, et al. Monitoring brain temperature by time-resolved near-infrared spectroscopy: pilot study. *J Biomed Opt* 2014; 19: 057005.

38. Fazel Bakhsheshi M, Diop M, St Lawrence K, et al. Quantitative measurement of cerebral blood flow during hypothermia with a time-resolved near-infrared technique. *Photonic Therapeutics and Diagnostics VIII* 2012; 8207: 82074R.

39. Fedotov IV, Solotenkov MA, Pochechuev MS, et al. All-optical brain thermometry in freely moving animals. *ACS Photonics* 2020; 7: 3353–3360.

40. Hong G, Diao S, Chang J, et al. Through-skull fluorescence imaging of the brain in a new near-infrared window. *Nat Photonics* 2014; 8: 723–730.

41. Shimosegawa E, Hatazawa J, Ibaraki M, et al. Metabolic penumbra of acute brain infarction: a correlation with infarct growth. *Ann Neurol* 2005; 57: 495–504.

42. Jiang M, Gao Y, Wu C, et al. The blood heat exchanger in intra-arterial selective cooling infusion for acute ischemic stroke: a computational fluid-thermodynamics performance, experimental assessment and evaluation on the brain temperature. *Comput Biol Med* 2022; 145: 105497.

43. Tichauer KM, Hadway JA, Lee TY, et al. Measurement of cerebral oxidative metabolism with near-infrared spectroscopy: a validation study. *J Cereb Blood Flow Metab* 2006; 26: 722–730.

44. Hashem M, Zhang Q, Wu Y, et al. Using a multimodal near-infrared spectroscopy and MRI to quantify gray matter metabolic rate for oxygen: a hypothermia validation study. *NeuroImage* 2020; 206: 116315.

45. Phelps ME, Huang SC, Hoffman EJ, et al. Validation of tomographic measurement of cerebral blood volume with C-11-labeled carboxyhemoglobin. *J Nucl Med* 1979; 20: 328–334.

46. Wang H, Wang B, Normoyle KP, et al. Brain temperature and its fundamental properties: a review for clinical neuroscientists. *Front Neurosci* 2014; 8: 307.

47. Tanos B and Kovács G. The ratio of body haematocrit to venous haematocrit in open heart surgery and estimation of the blood volume in the large and small vessels. *Acta Chir Acad Sci Hung* 1979; 20: 141–148.

48. Si J, Li M, Zhang X, et al. Cerebral tissue oximeter suitable for real-time regional oxygen saturation monitoring in multiple clinical settings. *Cogn Neurodyn* 2022; 17: 563–574.

49. Uludag K, Kohl M, Steinbrink J, et al. Cross talk in the Lambert-Beer calculation for near-infrared wavelengths estimated by monte carlo simulations. *J Biomed Opt* 2002; 7: 51–59.

50. Liu J, Yan Z, Pu Y, et al. Functional assessment of cerebral artery stenosis: a pilot study based on computational fluid dynamics. *J Cereb Blood Flow Metab* 2016; 37: 2567–2576.

51. Jiang M, Li M, Gao Y, et al. Design and evaluation of an air-insulated catheter for intra-arterial selective cooling infusion from numerical simulation and in vitro experiment. *Med Eng Phys* 2022; 99: 103736.

52. Jarrett CL, Shields KL, Broxterman RM, et al. Imaging transcranial doppler ultrasound to measure middle cerebral artery blood flow: the importance of measuring vessel diameter. *Am J Physiol Regul Integr Comp Physiol* 2020; 319: R33–r42. 2020/05/14.

53. Amukotuwa S, Straka M, Aksoy D, et al. Cerebral blood flow predicts the infarct core: new insights from contemporaneous diffusion and perfusion imaging. *Stroke* 2019; 50: 2783–2789. 2019/08/30. DOI: 10.1161/strokeaha. 119.026640.

54. Smith KD and Zhu L. Brain hypothermia induced by cold spinal fluid using a torso cooling pad: theoretical analyses. *Med Biol Eng Comput* 2010; 48: 783–791.

55. Yin L, Jiang H, Zhao W, et al. Inducing therapeutic hypothermia via selective brain cooling: a finite element modeling analysis. *Med Biol Eng Comput* 2019; 57: 1313–1322.

56. Lutz Y, Daschner R, Krames L, et al. Modeling selective therapeutic hypothermia in case of acute ischemic stroke using a 1D hemodynamics model and a simplified brain geometry. *Math Biosci Eng* 2019; 17: 1147–1167.

57. Meng L and Gelb AW. Cerebral oximetry: Three questions to ask. *Colombian Journal of Anesthesiology* 2015; 43: 52–56.

58. Lagendijk JJ. The influence of bloodflow in large vessels on the temperature distribution in hyperthermia. *Phys Med Biol* 1982; 27: 17–23.

59. Sukstanskii AL and Yablonskiy DA. Theoretical model of temperature regulation in the brain during changes in

functional activity. *Proc Natl Acad Sci U S A* 2006; 103: 12144–12149.

60. Polderman KH and Herold I. Therapeutic hypothermia and controlled normothermia in the intensive care unit: practical considerations, side effects, and cooling methods. *Crit Care Med* 2009; 37: 1101–1120.

61. Russell-Buckland J and Tachtsidis I. Developing a model to simulate the effect of hypothermia on cerebral blood flow and metabolism. *Adv Exp Med Biol* 2020; 1232: 299–306.

62. Baker WB, Balu R, He L, et al. Continuous non-invasive optical monitoring of cerebral blood flow and oxidative metabolism after acute brain injury. *J Cereb Blood Flow Metab* 2019; 39: 1469–1485.

63. Zeiner A, Klewer J, Sterz F, et al. Non-invasive continuous cerebral temperature monitoring in patients treated with mild therapeutic hypothermia: an observational pilot study. *Resuscitation* 2010; 81: 861–866.

64. Fahrenholtz SJ, Madankan R, Danish S, et al. Theoretical model for laser ablation outcome predictions in brain: calibration and validation on clinical MR thermometry images. *Int J Hyperthermia* 2018; 34: 101–111.

65. Li F, Gao J, Kohls W, et al. Perspectives on benefit of early and prereperfusion hypothermia by pharmacological approach in stroke. *Brain Circ* 2022; 8: 69–75.

66. Ma J, Li M, Zhang M, et al. Protection of multiple ischemic organs by controlled reperfusion. *Brain Circ* 2021; 7: 241–246.